Research Square

Preprints are preliminary reports that have not undergone peer review.
They should not be considered conclusive, used to inform clinical practice,
or referenced by the media as validated information.

Photothermal skyrmion tweezer: Programmable optical manipulation of topological quasiparticles

Min-Kyo Seo

minkyo_seo@kaist.ac.kr

Korea Advanced Institute of Science and Technology https://orcid.org/0000-0003-0618-3955

Jaeyu Kim

Korea Advanced Institute of Science and Technology

Seungmo Yang

Korea Research Institute of Standards and Science https://orcid.org/0000-0001-6501-3812

Dongha Kim

Korea Advanced Institute of Science and Technology https://orcid.org/0000-0002-6783-7273

Kyoung-Woong Moon

Korea research institute of standards and science https://orcid.org/0000-0002-2558-8985

Changsoo Kim

Korea Research Institute of Standards and Science https://orcid.org/0000-0003-1180-1703

Chanyong Hwang

Korea Research Institute of Standards and Science https://orcid.org/0000-0002-6612-7552

Physical Sciences - Article

Keywords:

Posted Date: June 6th, 2025

DOI: https://doi.org/10.21203/rs.3.rs-6460771/v1

License: This work is licensed under a Creative Commons Attribution 4.0 International License.
Read Full License

Additional Declarations: There is **NO** Competing Interest.

Version of Record: A version of this preprint was published at Nature Communications on December 13th, 2025. See the published version at https://doi.org/10.1038/s41467-025-66364-w.

Photothermal skyrmion tweezer: Programmable optical manipulation of topological quasiparticles

Jaeyu Kim[1]†, Seungmo Yang[2]†, Dongha Kim[1], Kyoung-Woong Moon[2], Changsoo Kim[2], Chanyong Hwang[2]§, and Min-Kyo Seo[1]*

[1]Nonlinear Quantum Photonics Laboratory, Department of Physics, KAIST, 291 Daehak-ro, Daejeon, 34141, Republic of Korea

[2]Quantum Technology Institute, Korea Research Institute of Standards and Science, 267 Gajeong-ro, Daejeon, 34113, Republic of Korea

†These authors contributed equally to this work.

§cyhwang@kriss.re.kr

*minkyo_seo@kaist.ac.kr

Abstract

Magnetic skyrmions, as topological quasiparticles, have shown great potential as information carriers for next-generation spintronic technologies, including memory, logic, and computing devices. While their non-trivial topological dynamics and interactions have been extensively explored, experimental control of individual skyrmions remains largely constrained to global stimuli such as electric currents, magnetic fields, and surface acoustic waves. Precise skyrmion positioning is further hindered by the skyrmion Hall effect and defect pinning. Here, we demonstrate high-precision trapping and transport of individual skyrmions via a photothermal potential well, thereby extending optical manipulation to the quasiparticle realm. Moreover, by integrating deterministic optical skyrmion creation and annihilation with photothermal and conventional electrical transport methods, we establish a fully programmable platform for systematic investigation of skyrmion dynamics and interactions. This approach opens new avenues towards robust, reversible and scalable architectures for future skyrmionic device applications and enriches studies of light–quasiparticle interactions in solid-state systems.

Introduction

Magnetic skyrmions are topologically nontrivial quasiparticles with a swirling spin configuration. Their topological protection against external perturbations[1] and high electrical mobility under low current density[2] make skyrmions strong candidates for energy-efficient information carriers in memory devices, logics, and unconventional computing architectures[3–8]. Another unique feature of skyrmions is the emergent magnetic field originating from their topology, which leads to distinct phenomena: the skyrmion Hall effect[9, 10] and the topological Hall effect[11, 12]. Suppressing the skyrmion Hall effect[13–15] is essential for efficient skyrmion transport, the topological Hall effect of electrons enables all-electrical skyrmion detection[16]. Recently, interactions of skyrmions with spin textures[17, 18], magnons[19, 20], and photons[21] have been reported leading to various emergent phenomena analogous to particle–antiparticle interactions, Landau levels, and band structure reconstruction. Thus, magnetic skyrmions provide a promising platform not only for demonstrating advanced spintronic devices and but also for the study of rich dynamics and physics of topological quasiparticles.

Precise and programmable control of individual skyrmions is crucial for both systematic investigations of their fundamental behavior and the reliable operation of skyrmionic devices. However, conventional electric current-driven techniques face significant limitations: the applied current affects multiple skyrmions simultaneously, reducing experimental selectivity and flexibility[22, 23]. Moreover, the electric transport and manipulation of magnetic skyrmions lack full spatial degrees of freedom due to the skyrmion Hall effect, which inherently distorts skyrmion trajectories[9, 10], and defect pinning, which leads to unpredictable stochastic motion[24, 25]. Alternative methods based on surface acoustic waves[26] or heat flow[27,28] present similar drawbacks. A recent approach utilizing a magnetic field gradient from a magnetic force microscopy probe[29] has demonstrated single-skyrmion manipulation, but it is limited by slow operation speed and the inability to simultaneously control and observe skyrmions.

Optical tweezers based on tightly focused laser beams provide noncontact and precise control of physical objects, ranging from microspheres[30, 31] and cells[32] to individual atoms[33, 34], advancing research in biology[35], chemistry[31, 36], and quantum sciences[37, 38]. By employing the optical tweezers, one

can assemble particle ensembles on demand, enabling experiments from two-particle interactions[36, 39] to many-body physics[40, 41]. However, despite their widespread applications, optical tweezers have so far been limited to manipulating real particles, with no prior experimental demonstration of their use for individual quasiparticles. In this work, we introduce optical manipulation and its advantages to skyrmions, magnetic topological quasiparticles in a spin system. A micron-scale photothermal potential well induced by focused laser incidence enables precise two-dimensional tweezing and isolation of a targeted single skyrmion, even overcoming the spin–orbit torque exerted by electric current pulses. Beyond conventional optical tweezers, the photothermal manipulation offers expanded functionality; we achieved deterministic creation and annihilation of a single skyrmion. By integrating this optical control with electrical transport, we establish fully programmable manipulation of skyrmions in two dimensions, laying the foundation for systematic investigation of skyrmion dynamics and interactions, and opening new avenues for quantum spintronic applications.

Photothermal trap for spin textures

At the core of our optical manipulation approach of individual skyrmions is the creation of a micrometer-scale photothermal potential well, generated by focused laser incidence (Fig. 1a). In magnetic systems with the presence of the interfacial Dzyaloshinskii–Moriya interaction (DMI) and the perpendicular magnetic anisotropy (PMA), the energy density of a chiral domain wall (DW) can be expressed as[42, 43] $U = 4\sqrt{AK_{\text{eff}}} - \pi D + \frac{\ln 2}{\pi}\mu_0 M_s^2 d$. Here, A is the exchange stiffness, K_{eff} is the effective PMA energy density per volume, D is the DMI energy density per surface, M_s is the saturation magnetization, and d is the film thickness. As the temperature increases, thermal fluctuations disrupt magnetic ordering, leading to a reduction in magnetic parameters[44]. According to Bloch's law, the saturation magnetization M_s decreases as the temperature approaches the Curie temperature, whereas A scales as[44] M_s^2. Similarly, both K_{eff} and D decrease due to thermal agitation[45, 46]. Therefore, whereas the term of the DMI energy density ($-\pi D$) increases, all the other energy terms contribute to a decrease in total energy density with increasing temperature. We measured K_{eff} and

M_S as a function of temperature and confirmed the dominant role of K_{eff} in the total energy density decrease as the temperature increases (Supplementary Information S1). A focused laser with a Gaussian beam profile locally heats the magnetic medium, generating a nonuniform temperature profile and thereby a photothermal potential well. This potential attracts adjacent skyrmions toward the laser-induced hot spot. By controlling the position of the laser beam, an individual skyrmion can be selectively dragged to a desired location or pinned at a specific point counteracting the motion induced by the electric current (Figs. 1b and 1c).

The photothermal effect induced by a high-intensity laser provides another opportunity to engineer individual skyrmions, enabling their selective creation or annihilation (Figs. 1d and 1e). When local heating exceeds a certain threshold temperature, the heated region demagnetizes. Because the heated area has much reduced coercivity, the local magnetization flips due to the small stray field from the surrounding magnetic domains and stabilizes into a skyrmion. Furthermore, by bringing one skyrmion close to another with our photothermal tweezer, we can make their DWs touch and cause the two skyrmions to merge into a single skyrmion. The size and shape of the merged skyrmion quickly converge to those of a typical skyrmion of the host magnetic medium.

In this work, we examined skyrmions in a multilayer stack comprising MgO (1 nm)/Ta (0.1 nm)/$Co_{20}Fe_{60}B_{20}$ (1.2 nm)/W (3 nm)/TaO_x (3 nm) on a Si/SiO_2 substrate (for further details, see the Methods section). The Ta layer was introduced to finely tune the PMA, while the W/CoFeB interface generates DMI strong enough to stabilize the skyrmionic textures. The W layer also supports spin–orbit torques for electric current-driven manipulation of skyrmions. A magneto-optical Kerr effect (MOKE) microscopy setup was used to visualize magnetization states in real time, where dark and light regions correspond to magnetization along the −z and +z directions, respectively.

A small perpendicular magnetic field of 2.56 Oe was applied to optimize the size and density of skyrmions. The resulting skyrmion diameter ranged from 2.0 to 5.0 μm, making them clearly resolvable under an optical microscope. The MOKE image (Fig. 1f) reveals sufficiently well-separated skyrmions, allowing individual manipulation without interference from neighboring skyrmions. A

skyrmion Hall effect measurement confirms the topological nature of our magnetic textures, validating them as magnetic skyrmions (Supplementary Information S2).

Skyrmion tweezers

We first demonstrate the use of the photothermal tweezer for dragging a single magnetic skyrmion along the laser beam's sweep direction (Fig. 2a). Once a single skyrmion is trapped within the beam spot by the photothermal potential, we move the sample relative to the fixed laser position and then the skyrmion is transported accordingly. This functionality enables precise control over the arrangement of skyrmions, enabling the creation of arbitrary patterns of skyrmions (Fig. 2b). The potential well landscape resulting from the temperature gradient is universal for any spin textures, regardless of their detailed distributions, as long as the PMA energy remains dominant. As a result, we can control magnetic DWs, not just individual skyrmions (Supplementary Information S3). From a topological perspective, a chiral DW with a semicircular shape carries a topological charge of ±1/2, often referred to as a "half skyrmion" [47,48]. We can extract a half skyrmion not only from bulk domain structures but also from a single skyrmion, by selectively dragging one of its ends (Supplementary Information S3).

The probability of stable skyrmion transport, defined as the likelihood that a target skyrmion remains intact without elongation or pinning to a local defect, was measured by varying the sweeping speed (v_{sw}) and laser beam power (Fig. 2c). Strong local material defects can pin or deform skyrmions during photothermal tweezing. For each combination of sweeping speed and laser beam power, we conducted 20 trials and recorded the success probability of transporting a single skyrmion over a distance of 10 μm. At a sweeping speed of 120 nm/s and a laser power of 6.02 mW, we were able to drag individual skyrmions with the high probability of 85%, which could be further enhanced by fabricating magnetic films with lower defect densities. As expected, the higher the sweeping speed, the lower the trapping probability, because the decline in trapping probability at higher sweeping speeds is attributed to skyrmion inertia, which hinders immediate coupling with the dynamic potential of the

optical tweezer.

The transport of skyrmions controlled by the photothermal tweezer can be understood as a thermally activated hopping process between intrinsic pinning sites in the magnetic film. The photothermal potential with a sufficiently strong driving force enables the skyrmion to overcome pinning potentials without deformation, but the probabilistic nature of creep motion determines the success of these "jumps," which depends on the driving duration. If the sweeping speed is too high, skyrmions do not have sufficient time to jump and follow the laser beam. The maximum sweeping speed allowable for jumps with the desired transport probability is inversely proportional to the probabilistic activation time, which follows the Arrhenius equation: $v_{sw} \propto \exp\left(-\frac{E_b}{k_B(T_0+\alpha P)}\right)$, where E_b is the activation energy barrier, k_B is the Boltzmann constant, P is the laser power, α is the heating coefficient, and T_0 is the ambient temperature. The results in Fig. 2c provide approximate but compelling support for this interpretation (Supplementary Information S4).

We also demonstrate that the photothermal potential well can pin a selected skyrmion at a desired position, preventing displacement due to external electric current injection. We tracked the motion of several skyrmions under electric current pulse injection (Fig. 3a): free skyrmions (colored blue, yellow, and orange), a skyrmion pinned at a persistent intrinsic defect (colored green), and a selected skyrmion trapped by the photothermal tweezer (colored red). While all free skyrmions move along the direction of the injected current pulses, the photothermally trapped skyrmion, confined by a 6.5 mW laser, remains stationary, similar to the skyrmion pinned at the defect site. The displacement of the skyrmions from their initial positions was quantitatively measured (Fig. 3b). While the laser for the photothermal potential was on, for the first five current pulses (N = 0–5), the displacement of both the photothermally pinned and defect-pinned skyrmions was minimal. By contrast, free skyrmions moved 2.4 μm per pulse on average. We turned off the laser before applying the sixth pulse (N = 6), after which the previously photothermally pinned skyrmion started to move freely, while the defect-pinned skyrmion remained stationary. Here, the applied electric pulses were square-shaped with 7.79×10^9 A/m^2 current density and 100 ms duration.

Higher laser power enhances the depth of photothermal potential well, thereby increasing the skyrmion resistance to the external driving current. We statistically investigated the displacement of a skyrmion induced by a single electric pulse depending on the laser power and the current density. Figure 3c shows box plots of the first and third quartiles, along with the median, based on 20 trials per condition. To minimize inhomogeneous spatial variations in the intrinsic pinning potential, we examined skyrmions located at the same position (for further details, see the Methods section). Skyrmion transport by electric pulses exhibits a threshold behavior, in which the total pinning potential, the sum of the intrinsic and photothermal potentials, must be overcome. Without laser pinning, skyrmions remain pinned unless the current density exceeds a threshold of 4.24×10^9 A/m^2 (blue dashed line). When the laser pinning is turned on, the additional photothermal potential well increases the threshold current density required for skyrmion motion to 4.56×10^9 A/m^2 at a laser power of 4.14 mW (orange dashed line) and to over 5.19×10^9 A/m^2 at 5.06 mW. This result demonstrates the capability of the photothermal effect to locally engineer the potential landscape for skyrmions, offering precise control over their dynamics and stability.

Fully programmable skyrmion manipulation

The photothermal effect enables the deterministic creation of an isolated skyrmion at a desired position. Localized heating from the focused laser beam reduces the material's magnetic properties, including magnetization and coercivity, and lowers the energy barrier for magnetization reversal. The flipped magnetization is stabilized by the stray field from neighboring magnetizations[49]. The resulting bubble domain adopts a skyrmionic texture, because the equilibrium state of DWs in our sample is chiral[50, 51]. The process of optical skyrmion generation is shown in Fig. 4a. The initial state of the uniformly magnetized domain is shown in the first panel, with the red circle indicating the position of the laser beam in advance. The deterministic creation of a single skyrmion at the irradiated location is shown in the second panel. The generated skyrmion has the same size and shape as the original skyrmions and, as shown in the third panel of Fig. 4a, it exhibits identical motion when we applied an

electric pulse (3.14×10^9 A/m^2 current density and 100 ms duration). Next, the skyrmion Hall effect for optically created skyrmions was measured, confirming their deflection from the direction of the injected current pulse and validating their topological nature and nonzero winding number (Supplementary Information S2).

The probability of skyrmion generation as a function of the incident laser power is quantified in Fig. 4b. The laser was irradiated for 1 s, and the probability was evaluated over 20 trials at different locations for each power level. Below 3 mW, no skyrmions were generated, whereas above 4 mW, the skyrmion formation probability increased dramatically, ultimately leading to deterministic creation. This result demonstrates that photothermal skyrmion generation requires a laser power exceeding a critical threshold. Conventional skyrmion creation methods using external magnetic fields[50, 51], ultrafast lasers[52], and electrical current pulses[49], are limited to either generating a large number of skyrmions stochastically or confining their formation to predefined locations, such as electrodes or tracks. By contrast, photothermal generation enables precise and deterministic skyrmion creation at arbitrary positions, making it a versatile tool for potential quantum and spintronic applications.

By integrating the techniques outlined above, we demonstrated fully programmable control over the motion of an individual skyrmion through successive operations of the photothermal tweezer. As shown in Fig. 4c, the comprehensive manipulation, including skyrmion creation, pinning, transport, and annihilation, within a 5 × 5 cell array was experimentally demonstrated. Each unit cell measures 4.3 μm × 4.3 μm, a spacing determined by the typical displacement of a skyrmion induced by an electrical pulse (3.14×10^9 A/m² current density and 100 ms duration). Starting from an initial configuration with two preexisting skyrmions (colored blue), and using the photothermal effects, a new skyrmion (colored red) was created at a target position. The created skyrmion was pinned with a photothermal tweezer, whereas the two preexisting skyrmions were shifted by an electric pulse. Subsequently, the created skyrmion was transported independently to other cells using the photothermal tweezer. Unlike electrical current-driven motion, which is restricted to predetermined directions, the photothermal tweezer enables flexible two-dimensional skyrmion positioning with high spatial

precision. Finally, the created skyrmion was dragged to a preexisting skyrmion, and as they approached closer, the DWs separating them become demagnetized by the thermal effect. This operation provided enough energy to break the topological barrier merging them into a single skyrmion. The ability to control the birth, movement, and annihilation of individual skyrmions shows the potential of advanced two-dimensional spintronic application.

Concluding Remarks

In this study, we demonstrated the optical manipulation of skyrmions, magnetic quasiparticles, using a micrometer-scale photothermal potential well generated by a focused laser beam. The photothermal potential, which effectively attracts magnetic chiral DWs, enables precise tweezing and pinning of an individual skyrmion at a desired position, even overcoming transport driven by electric current injection. The properties and performance of the photothermal skyrmion tweezer, as a function of incident laser power and sweeping speed, were quantitatively investigated. The photothermal effect can also create or annihilate a single skyrmion. By combining collective electric transport for large-scale skyrmion motion with targeted photothermal manipulation of a selected one, efficient, fully programmable control of skyrmions in two dimensions was achieved. We expect that recent advances in wavefront engineering using spatial light modulators will further enhance the versatility of the photothermal potential, facilitating modulation of its distribution and dynamic motion to enable a more sophisticated study of interactions and coupling with other spin textures. Moreover, the programmable creation, manipulation, and annihilation of individual skyrmions will expand the functionalities of existing skyrmionic devices, such as probabilistic computing architectures, multiplexers, and reconfigurable logic gates.

References

1. Je, S.-G. et al. Direct demonstration of topological stability of magnetic skyrmions via topology manipulation. *ACS Nano* **14**, 3251–3258 (2020).
2. Wang, K., Bheemarasetty, V., Duan, J., Zhou, S. & Xiao, G. Fundamental physics and applications of skyrmion: A review. *J. Magn. Magn. Mater.* **563,** 169905 (2022).
3. G. Yu, et al. Room-temperature skyrmion shift device for memory application. *Nano Lett.* ***17***, 261–268 (2017).
4. Luo, S. et al. Reconfigurable skyrmion logic gates. *Nano Lett.* **18**, 1180–1184 (2018).
5. Zázvorka, J. et al. Thermal skyrmion diffusion in a reshuffle device. *Nat. Nanotechnol.* **14**, 658–661 (2019).
6. Song, K. M. et al. Skyrmion-based artificial synapses for neuromorphic computing. *Nat. Electron.* **3**, 148–155 (2020).
7. Beneke, G. et al. Gesture recognition with Brownian reservoir computing using geometrically confined skyrmion dynamics. *Nat. Commun.* **15**, 8103 (2024).
8. Yokouchi, T. et al. Pattern recognition with neuromorphic computing using magnetic field-induced dynamics of skyrmions. *Sci. Adv.* **8**, eabq5652 (2022).
9. Litzius, K. et al. Skyrmion Hall effect revealed by direct time-resolved X-ray microscopy. *Nat. Phys.* **13**, 170–175 (2017).
10. Jiang, W. et al. Direct observation of the skyrmion Hall effect. *Nat. Phys*. **13**, 162–169 (2017).
11. Kurumaji, T. et al. Skyrmion lattice with a giant topological Hall effect in a frustrated triangular-lattice magnet. *Science* **365**, 914–918 (2019).
12. Shao, Q. et al. Topological Hall effect at above room temperature in heterostructures composed of a magnetic insulator and a heavy metal. *Nat. Electron.* **2**, 182–186 (2019).
13. Hirata, Y. et al. Vanishing skyrmion Hall effect at the angular momentum compensation temperature of a ferrimagnet. *Nat. Nanotechnol.* **14**, 232–236 (2019).
14. Pham, V. T. et al. Fast current-induced skyrmion motion in synthetic antiferromagnet. *Science* **384**, 307–312 (2024).
15. Dai, B. et al. Electric field manipulation of spin chirality and skyrmion dynamic. *Sci. Adv.* **9**, eade6836 (2023).
16. Maccariello, D. et al. A. Fert. Electrical detection of single magnetic skyrmions in metallic multilayers at room temperature. *Nat. Nanotechnol.* **13**, 233–237 (2018).
17. Zheng, F. et al. Skyrmion–antiskyrmion pair creation and annihilation in a cubic chiral magnet. *Nat. Phys.* **18**, 863–868 (2022).
18. Du, H. et al. Interaction of individual skyrmions in a nanostructured cubic chiral magnet. *Phys. Rev. Lett.* **120**, 197203 (2018).
19. Weber, T. et al. Topological magnon band structure of emergent Landau levels in a skyrmion lattice. *Science* **375**, 1025–1030 (2022).
20. Mochizuki, M. et al. Thermally driven ratchet motion of a skyrmion microcrystal and topological magnon Hall effect. *Nat. Mater.* **13**, 241-246 (2014).
21. Kato, Y. D., Okamura, Y., Hirschberger, M., Tokura, Y. & Takahashi, Y. Topological magneto-optical effect from skyrmion lattice. *Nat. Commun.* **14**, 5416 (2023).
22. Vélez, S. et al. Current-driven dynamics and ratchet effect of skyrmion bubbles in a ferrimagnetic

insulator. *Nat. Nanotechnol.* **17**, 834–841 (2022).

23. Ji, Y. et al. Direct observation of room-temperature magnetic skyrmion motion driven by ultra-low current density in van der Waals ferromagnets. *Adv. Mater.* **36**, 2312013 (2024).
24. Song, M. et al. Universal hopping motion protected by structural topology. *Adv. Mater.* **34**, 2203275 (2022).
25. Peng, L. et al. Dynamic transition of current-driven single-skyrmion motion in a room-temperature chiral-lattice magnet. *Nat. Commun.* **12**, 6797 (2021).
26. Chen, R. et al. creation and motion of skyrmions with surface acoustic wave. *Nat. Commun.* **14**, 4427 (2023).
27. Yu, X. et al. Real-space observations of 60-nm skyrmion dynamics in an insulating magnet under low heat flow. *Nat. Commun.* **12**, 5079 (2021).
28. Qin, G. et al. Dynamics of magnetic skyrmions driven by a temperature gradient in a chiral magnet FeGe. *Phys. Rev. B* **106**, 024415 (2022).
29. Casiraghi, A. Individual skyrmion manipulation by local magnetic field gradients. *Commun. Phys.* **2**, 145 (2019).
30. Curtis, J. E., Koss, B. A. & Grier., D. G. Dynamic holographic optical tweezers. *Opt. Commun.* **207**, 169–175 (2002).
31. Black, J. W., Kamenetska, M., Ganim, Z. An optical tweezers platform for single molecule force spectroscopy in organic solvents. *Nano Lett.* **17**, 6598–6605 (2017).
32. Wang, X. et al. Sun. Enhanced cell sorting and manipulation with combined optical tweezer and microfluidic chip technologies. *Lab Chip* **11**, 3656–3662 (2011).
33. Schlosser, N., Reymond, G., Protsenko, I. & Grangier., P. Sub-Poissonian loading of single atoms in a microscopic dipole trap. *Nature* **411**, 1024–1027 (2001).
34. Kim, H. et al. In situ single-atom array synthesis using dynamic holographic optical tweezers. *Nat. Commun.* **7**, 13317 (2016).
35. Bustamante, C. J., Chemla, Y. R., Liu, S. & Wang, M. D. Optical tweezers in single-molecule biophysics. *Nat. Rev. Methods Primers* **1**, 25 (2021).
36. Liu, L. R. et al. Building one molecule from a reservoir of two atoms. *Science* **360**, 900–903 (2018).
37. Shadmany, D. et al. Cavity QED in a high NA resonator. *Sci. Adv.* **11**, eads8171 (2025).
38. Holland, C. M., Lu, Y. & Cheuk, L. W. On-demand entanglement of molecules in a reconfigurable optical tweezer array, *Science* **382**, 1143–1147 (2023).
39. Cheuk, L. W. et al. Observation of collisions between two ultracold ground-state CaF molecules. *Phys. Rev. Lett.* **125**, 043401 (2020).
40. Ebadi, S. et al. Quantum phases of matter on a 256-atom programmable quantum simulator. *Nature* **595**, 227–232 (2021).
41. Bornet, G. et al. Scalable spin squeezing in a dipolar Rydberg atom array. *Nature* **621**, 728–733 (2023).
42. Gross, I. et al. Direct measurement of interfacial Dzyaloshinskii-Moriya interaction in *X*|CoFeB|MgO heterostructures with a scanning NV magnetometer (*X* =Ta,TaN, and W). *Phys. Rev. B* **94**, 064413 (2016).
43. Yang, S. et al. Magnetic skyrmion transistor gated with voltage-controlled magnetic anisotropy. *Adv. Mater.* **35**, 2208881 (2023).
44. Chikazumi, S. *Physics of Ferromagnetism* (Oxford, 2009).

45. Lee, K-M., Choi, J.W., Sok, J. & Min. B-C. Temperature dependence of the interfacial magnetic anisotropy in W/CoFeB/MgO. *AIP Adv.* **7**, 065107 (2017).

46. Schlotter, S., Agrawal, P., Beach & G. S. D. Temperature dependence of the Dzyaloshinskii-Moriya interaction in Pt/Co/Cu thin film heterostructures. *Appl. Phys. Lett.* **113**, 092402 (2018).

47. Jena, J. et al. Observation of fractional spin textures in a Heusler material. *Nat. Commun.* **13**, 2348 (2022).

48. Yang, S. et al. Control of Half-Skyrmion Hall Effect and Its Application to Adder-Subtractor. *Adv. Quantum Technol.* **4**, 2000060 (2021).

49. Yang, S. et al. Electrical generation and deletion of magnetic skyrmion-bubbles via vertical current injection. *Adv. Mater.* **33**, 2104406 (2021).

50. Moon, K.-W. et al. Universal method for magnetic skyrmion bubble generation by controlling the stripe domain instability. *NPG Asia Mater.* **13**, 20 (2021).

51. Yang, S. et al. Magnetic field magnitudes needed for skyrmion generation in a general perpendicular magnetized film. *Nano Lett.* **22**, 8430–8436 (2022).

52. Je, S.-G. et al. Creation of magnetic skyrmion bubble lattices by ultrafast laser in ultrathin films. *Nano Lett.* **18**, 7362–7371 (2018).

Methods

Sample fabrication

The magnetic thin films, consisting of an MgO (1 nm) / Ta (0.1 nm) / $Co_{20}Fe_{60}B_{20}$ (1.2 nm) / W (3 nm) / TaO_x (3 nm) stack, were deposited on a Si/SiO_2 substrate by DC/RF magnetron sputtering. After deposition, the sample underwent a post-annealing process at 350 °C for 1 hour under a 1×10^{-7} Torr vacuum. For electrical transport measurements of magnetic skyrmions, electrodes composed of Ti (2 nm) / Au (50 nm) were fabricated using photo-lithography and a lift-off process. We prepared two identical samples grown under the same fabrication conditions. Sample #1 was used for the experiments shown in Figs. 2a and 2c, as well as Figs. 3a and 3b, while Sample #2 was used for those in Fig. 2b, Fig. 3c, and Fig. 4. This separation was intended to avoid inaccuracies due to potential sample degradation from repeated experiments used for statistical analysis. We confirmed the equivalence of magnetic properties of the two samples (see Supplementary Information S1 for more details).

Experimental setup

Local photo-thermal heating was achieved using a focused 638 nm continuous-wave (CW) laser. The diameter of the focused laser beam was 2.4 μm, comparable to the typical skyrmion size in the magnetic films studied. The magneto-optical Kerr effect (MOKE) microscopy setup for real-time skyrmion motion measurements consisted of a 530 nm light-emitting diode (LED) for illumination and an electron-multiplying charge-coupled device (iXon DU-897). A piezoelectric translation stage was used to precisely move the sample in two dimensions, allowing the focused beam to sweep relative to the sample. Custom-built electromagnets were used to apply both in-plane and out-of-plane magnetic fields simultaneously. For all experiments shown in the main manuscript, an out-of-plane magnetic field of 2.56 Oe was applied to tune skyrmion size. An in-plane magnetic field was applied only during the initial nucleation of skyrmions from the stripe domain state across the sample and was then set to zero during all other measurements.

Photothermal pinning measurement

For statistical analysis of the motion of photo-thermally pinned skyrmions per electrical current pulse (Fig. 3c in the main text), we examined skyrmions created at the same predefined position and minimized differences arising from spatial inhomogeneity across the sample. The photo-thermal effect enabled the deterministic creation of a skyrmion at a fixed position, carefully selected to avoid any persistent intrinsic defects that might skew the statistical results. Instances where the target skyrmion was annihilated by high-current-density electrical pulses were excluded from the statistical analysis. The motion of skyrmions was tracked in real time using the MOKE microscope and quantitatively analyzed using the TrackMate plugin in ImageJ software (National Institutes of Health and the Laboratory for Optical and Computational Instrumentation, University of Wisconsin).

Data Availability

The data that support the findings of this study are available from the corresponding author upon reasonable request.

Acknowledgements

This work was supported by KAIST Cross-Generation Collaborative Lab project; the National Research Foundation of Korea (NRF) (RS-2024-00350185, RS-2024-00408271); Nano & Material Technology Development Program through the National Research Foundation of Korea (NRF) funded by Ministry of Science and ICT(RS-2024-00451261); National Research Council of Science & Technology (NST) grant by the Korea government (MSIT) (No. GTL24041-000). We thank T.-S. Ju for his support in sample preparation; K.-J. Kim and K.-J. Lee for their valuable discussions.

Author contributions: J.K. and M.K.S. conceived the project. S. Y. and K.W. M. fabricated the sample. J.K. performed all the measurements and analysis. J.K., S. Y., and M.K.S. analysed the data. J.K. and M.K.S. wrote the manuscript with the assistance of all other authors.

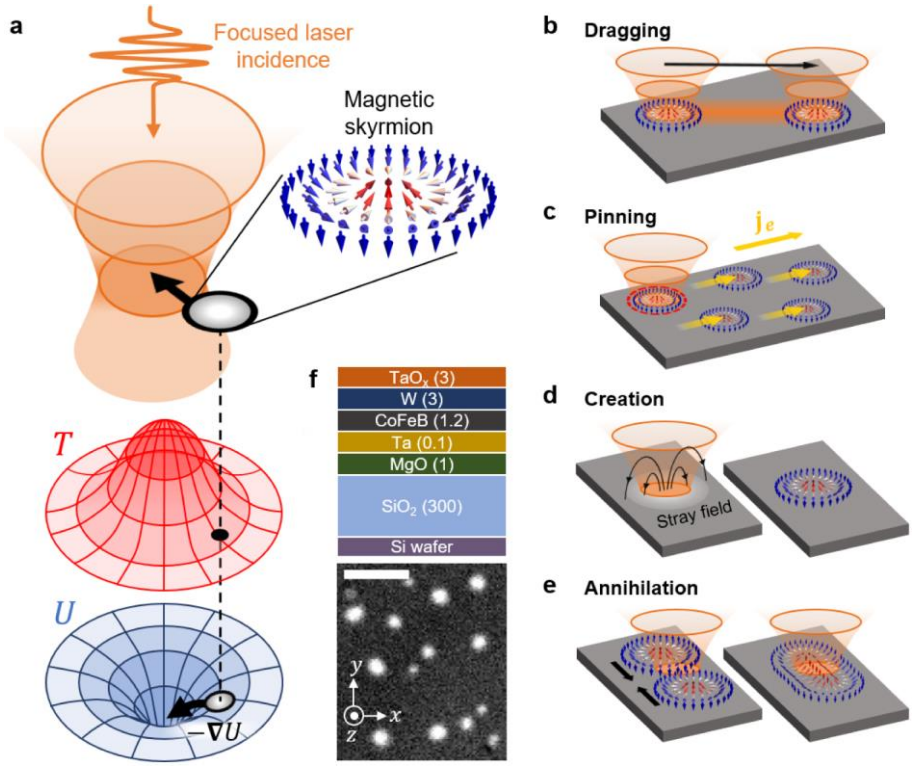


Fig. 1. Photothermal manipulation of individual magnetic skyrmions. **a**, Illustration of the temperature (T) and potential energy (U) distributions created by the photothermal effect of focused laser incidence on the magnetic film. **b–e**, Schematics of the photothermal dragging, pinning, creation, and annihilation of an individual skyrmion. **f**, Top: Structure of the employed magnetic film, with the numbers in parentheses indicating the thickness of each layer in nanometers. Bottom: Magneto-optical Kerr effect microscope (MOKE) image of spontaneously generated magnetic skyrmions. Scale bar, 10 μm.

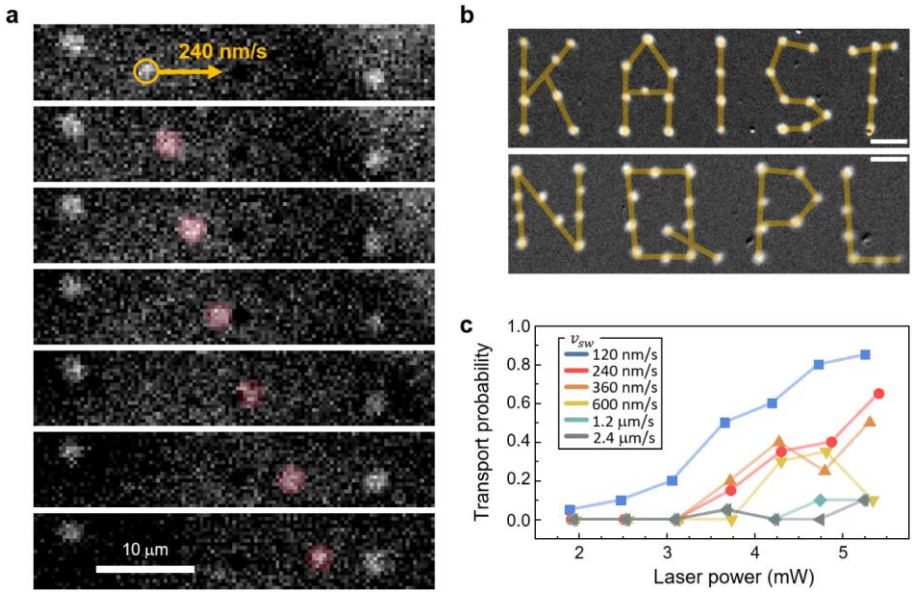


Fig. 2. Transport and arrangement of individual magnetic skyrmions using the photothermal tweezer. a, Photothermal tweezing of an isolated single magnetic skyrmion (colored in red). **b**, On-demand arrangement of skyrmions by a photothermal tweezer forming the patterns “KAIST” (upper panel) and “NQPL” (lower panel). Scale bar, 10 μm. **c**, Probability of successfully transporting a single skyrmion over a 10 μm distance as a function of the incident laser power and sweeping speed, based on 20 trials for each condition.

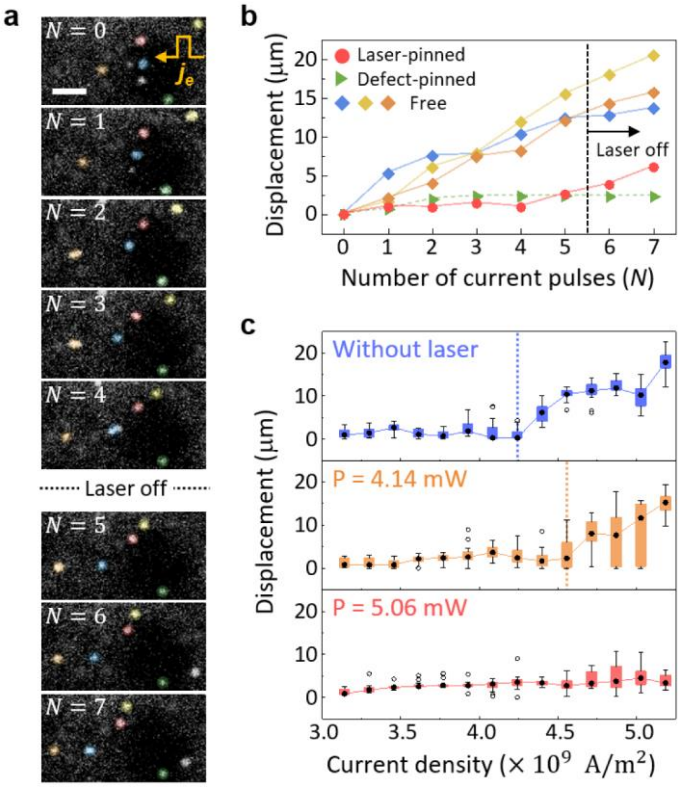


Fig. 3. Selective photothermal pinning of a magnetic skyrmion. **a**, Snapshots of magnetic skyrmions under successive electric current pulses. *N* denotes the number of current pulses applied from the initial state ($N = 0$). Individual skyrmions are highlighted in different colors for clarity: the red-shaded skyrmion was photothermally pinned, the green-shaded skyrmion was pinned at an intrinsic defect site, and the other skyrmions were free to move under electric current pulses. Scale bar, 10 μm. **b**, Displacements of the skyrmions shown in (a) as a function of the number of applied current pulses. The pinning laser was turned off between the fifth and sixth pulses. **c**, Statistical analysis of skyrmion displacement induced by a single current pulse, with and without laser pinning ($P = 4.14$ mW and 5.06 mW). The data from 20 trials per condition are presented by box plots, showing the first and third quartiles, the median as a solid dot, and outliers as empty circles outside the 1.5 interquartile range.

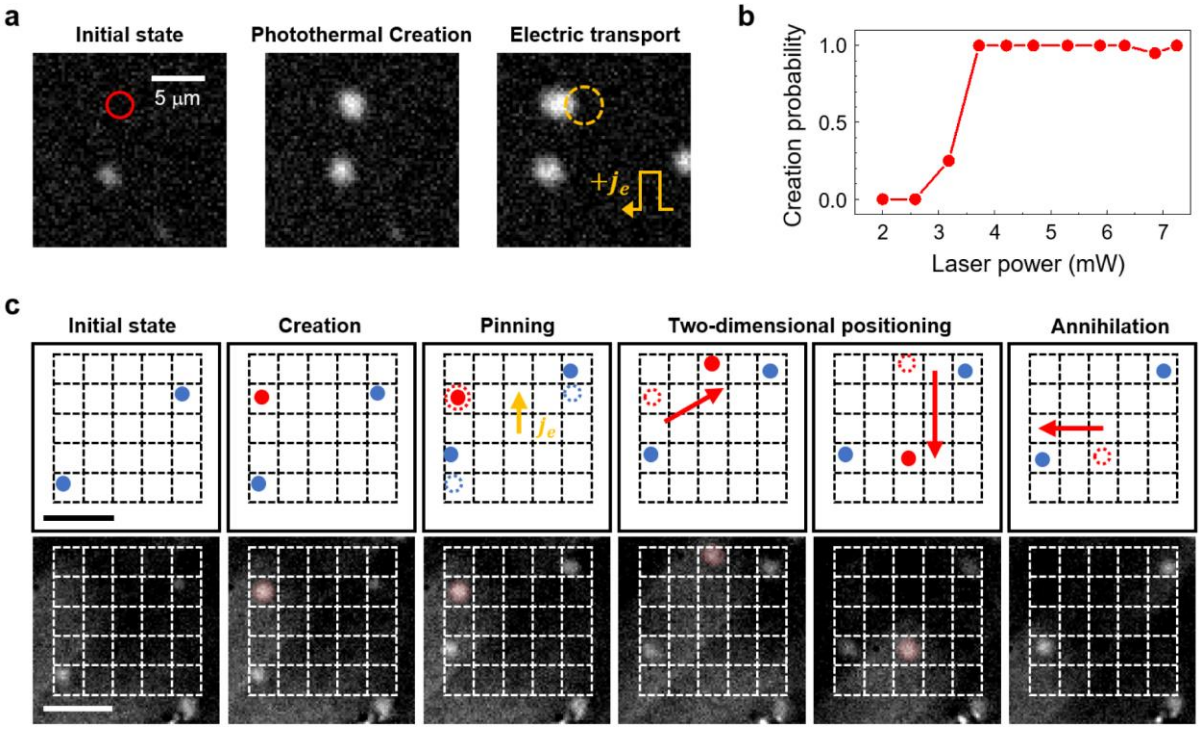


Fig. 4. Fully programmable control of a magnetic skyrmion using a photothermal tweezer. a, Photothermal creation of a skyrmion and its subsequent electrical drift. **b**, Probability of skyrmion creation as a function of the incident laser power. **c**, Programmed skyrmion motion under successive operation based on the photothermal tweezer, including its creation, pinning, positioning, and annihilation. Scale bar, 10 μm.

Supplementary Files

This is a list of supplementary files associated with this preprint. Click to download.

- Supplementaryinformation.docx